

Microstructure and texture evolution of novel Cu–10Ni–3Al–0.8Si alloy during hot deformation

Leinuo Shen and Zhou Li^{a)}

Department of Material Physics and Chemistry, School of Materials Science and Engineering, Central South University, Changsha 410083, Hunan, China

Qiyi Dong

Department of Material Physics and Chemistry, School of Materials Science and Engineering, Central South University, Changsha 410083, Hunan, China; and State Key Laboratory of Powder Metallurgy, Central South University, Changsha 410083, Hunan, China

Zhu Xiao

Department of Material Physics and Chemistry, School of Materials Science and Engineering, Central South University, Changsha 410083, Hunan, China

Chang Chen

Department of Metallic Materials, School of Materials Science and Engineering, Heifei University of Technology, Heifei 230009, Anhui, China

(Received 19 December 2015; accepted 1 March 2016)

The influence of temperature and strain rate on hot deformation behavior and microstructure of Cu–10Ni–3Al–0.8Si alloy was investigated. The true stress increased rapidly initially until it approached the peak values. The peak value of true stress and the Zener–Hollomon parameter decreased with the increase of temperature and the decrease of strain rate. The thermal activation energy of the alloy was about 396.57 kJ/mol, the processing map was established and the appropriate compression temperature was between 900 and 950 °C. The $\langle 001 \rangle$ and $\langle 011 \rangle$ fiber texture was the main type of texture. The increase of temperature or strain rate accelerated the formation of $\langle 001 \rangle$ fiber texture. Dynamic recrystallization nucleated and deformation bands formed at 750 °C. Recrystallization was accelerated with the increase of temperature and the decrease of Zener–Hollomon parameter. Both continuous recrystallization resulting from dynamic recovery and dynamic discontinuous recrystallization were softening mechanisms.

I. INTRODUCTION

Cu–Be alloys have been the most widely used elastic copper alloy because of their combination of super high strength, good electrical conductivity, excellent wear resistant, and corrosion resistant.^{1–3} The hardness of commercial Cu–2Be alloy was over 350 HV after cold rolled by 37% and aged at 275 °C for 2 h.³ Recently, a series of elastic copper alloy such as Cu–Ni–Sn, Cu–Ti, Cu–Ni–Si, and Cu–Ni–Al alloys have been developed to substitute the toxic Cu–Be alloys. It was reported that hardness and tensile strength of Cu–10Ni–3Al–0.8Si alloy could reach up to 380 HV and 1124 MPa, which made Cu–Ni–Al alloy the most promising elastic material in a series of applications, such as springs, bearings, tubes, and gears.^{4,5} Hot deformation processes such as forging, rolling, and extrusion, are applied to manufacture bulk copper alloys. The deformation ability of copper alloys influences their microstructures and properties. The hot compression tests are used to simulate

the actual forming operations in terms of stress state and strain rate, to select the optimal condition with excellent workability, identify microstructure, and crystal orientation.⁶ During hot compression, deformation bands (DBs) and textures form due to the heavy deformation, while dynamic recovery and dynamic recrystallization occur because of relatively high temperature, resulting in the changes of the texture and microstructure.^{7–9} However, the evolution of microstructure and crystal orientation of Cu–Ni–Al–Si alloy during hot compression process have not been fully investigated.

In this paper, the hot deformation behavior of Cu–10Ni–3Al–0.8Si alloy was studied. The influence of temperature and strain rate on microstructure and crystal orientation was also investigated. The processing map was established and the optimal condition of this alloy for processing was determined.

II. EXPERIMENTAL PROCEDURE

A. Material preparation

The designed Cu–10Ni–3Al–0.8Si alloy (wt%) was prepared in an intermediate frequency furnace. After the

Contributing Editor: Jürgen Eckert

^{a)}Address all correspondence to this author.

e-mail: lizhou6931@163.com

DOI: 10.1557/jmr.2016.104

surface defects were removed, the ingot was isothermal treated at 920 °C for 2 h and then cut into cylinder samples with dimension of $\Phi 8 \text{ mm} \times 12 \text{ mm}$ by a wire electrical discharge machining.

B. The hot compressing tests

The hot deformation experiments were conducted on a Gleeble-3500 thermal simulator (Dynamic Systems Inc., Redmond, Washington) under Ar atmosphere. The experimental temperatures were 750, 800, 850, 900, and 950 °C, and the strain rates were 0.01, 0.1, 1, and 5 s^{-1} , respectively. The lubricants were a mixture solution of graphite, No. 45 engine oil and tricresyl nitrate ester with volume ratio of 15:4:1. All the samples were hot compressed by 60% and then quenched in water. The friction between the samples and machine can be reduced by application of lubricant, but cannot be eliminated completely. To obtain accurate true stress–strain curves and thermal activation energy, the model based on the upper-bound theorem was applied to estimate the friction during hot compression tests.¹⁰ The amended true stress can be calculated as following^{11,12}:

$$\sigma = \frac{P \left(\frac{2mR}{h} \right)^2}{2 \left[\exp \left(\frac{2mR}{h} \right) - \frac{2mR}{h} - 1 \right]}, \quad (1)$$

$$R = R_0 \sqrt{\frac{h_0}{h}}, \quad (2)$$

$$m = \frac{3\sqrt{3}R_1(R_M - R_1)}{3R_1h - 2h_1(R_M - R_1)}, \quad (3)$$

$$R_1 = \sqrt{3 \frac{h_0}{h_1} R_0^2 - 2R_M^2}, \quad (4)$$

where, P is the initial true stress, m is the friction factor; h_0 is the initial height of the sample; Δh is the displacement; h is the instantaneous height of the sample, and $h = h_0 - \Delta h$; h_1 is the height of the sample after compression; R_0 is the initial radius of the sample; R is the instantaneous radius of the sample, R_M is the maximum radius of the sample after compression; and R_1 is the radius of the bottom of sample.

C. Microstructure observation

The optical microstructure (OM) observation was conducted on a Leica optical microscope (Leica Microsystems, Wetzlar, Germany). Texture measurements were carried out on a Bruker D8 Discover machine (Bruker Corporation, Karlsruhe, Germany). Inverse pole figures of the planes {200}, {220}, and {222} were measured. Defocusing correction was carried out by a random specimen of pressed and sintered high purity Cu powder.

The electron backscatter diffraction (EBSD) observation was performed on a FEI Sirion 200 scanning electron microscope (FEI Company, Eindhoven, The Netherlands). The results were analyzed using the Orientation Imaging Microscopy (OIM) Analysis 5 software. The samples for texture measurements and EBSD observation were sectioned parallel to the compression axis along the direction of centerline, then abraded and electrolytic polished in a mixing solution of H_3PO_4 and ethanol with a ratio of 1:1 at room temperature. Transmission electron microscopy (TEM) observation and selected area diffraction patterns (SADP) were performed on a JEM-2100F (JEOL Ltd., Tokyo, Japan), with the operation voltage of 200 kV. The specimens for TEM observation were mechanically reduced to 0.06 mm and then electron-polished by the standard twin-jet electro-polishing method using the methanol-nitric acid solution with a ratio of 3:1 at a temperature between -20 and -30 °C.

III. RESULTS AND DISCUSSION

A. Flow stress behavior

The true stress–strain curves of isothermal treated Cu–10Ni–3Al–0.8Si alloy are shown in Fig. 1. The results indicated that true stress increased rapidly initially until the peak values approached. The work hardening played the main role at the initial stage of compression. A plenty of dislocations were introduced during hot compressing. Those dislocations were able to interact with secondary phases or tangle with each other, resulting in the increase of strength and true stress. As hot compressed at low temperature (between 750 and 800 °C), the samples broke as true strain increased. Increasing compression temperature, the peak value of true stress decreased and the true stress remained its peak value as true strain further increased. Except for work hardening, recovery and recrystallization also occurred during hot compression process and decreased the amount of dislocation and crystal defects, resulting in the decrease of true stress. The effect of both work hardening, recovery and recrystallization almost kept balance, as a result, the true stress remained unchanged. Recovery and recrystallization were thermal active processes, which would be promoted with evaluated compression temperature and decrease of strain rate (increase of hot compressing time), resulting in the decrease of resisting force of hot compression. Therefore, the peak value of true stress slightly decreased as temperature increased and strain rate decreased.

According to the flow stress–strain model,¹³ the influence of strain rate, thermal activation energy, and hot compression temperature on true stress can be explained as following:

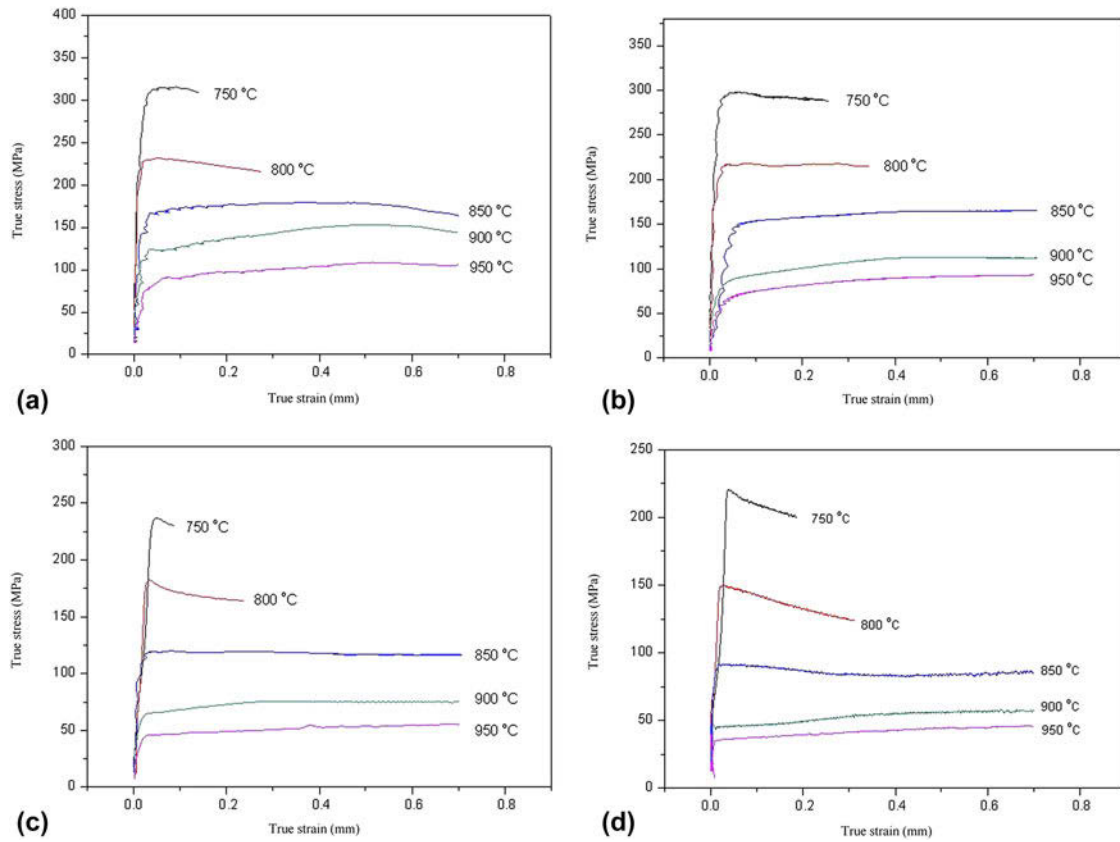


FIG. 1. True stress–strain curves of Cu–10Ni–3Al–0.8Si alloy with different strain rates and temperatures (a) 5 s^{-1} ; (b) 1 s^{-1} ; (c) 0.1 s^{-1} ; (d) 0.01 s^{-1} .

$$\dot{\epsilon} = AF(\sigma) \exp\left(-\frac{Q}{RT}\right), \quad (5)$$

where, $\dot{\epsilon}$ is strain rate; σ is the flow stress; Q is thermal activation energy; T is hot compression temperature; A is a constant, and R is the gas constant.

And $F(\sigma)$ is closely related to the stress¹⁴:

$$\begin{cases} F(\sigma) = \exp(\beta\sigma) & \alpha\sigma > 1.2 \\ F(\sigma) = \sigma^n & \alpha\sigma < 0.8 \\ F(\sigma) = [\sinh(\alpha\sigma)]^n & \text{for all the values} \end{cases} \quad (6)$$

here, n , β , and α are constants, while $\alpha = \beta/n$.

Combining Eqs. (5) and (6), the thermal activation energy can be calculated as following:

$$Q = R \left\{ \frac{\partial \ln \dot{\epsilon}}{\partial \ln [\sinh(\alpha\sigma)]} \right\} \left\{ \frac{\partial \ln [\sinh(\alpha\sigma)]}{\partial (1/T)} \right\} = Rn'S, \quad (7)$$

where, n' and S are constants.

Figure 2 presents the plots of $\ln \dot{\epsilon}$ versus σ , $\ln \dot{\epsilon}$ versus $\ln \sigma$, $\ln [\sinh(\alpha\sigma)]$ versus $\ln \dot{\epsilon}$ and $1000/T$ versus $\ln [\sinh(\alpha\sigma)]$. The value of β , n , n' , and S was obtained by

calculating the average value of the slope of the straight lines in each figure. The value of β , n , n' , and S was about 0.055, 8.09, 5.81, and 8.21, respectively, while the value of α and $\ln A$ is 0.0068 and 40.76, respectively. Therefore, the calculated thermal activation energy of Cu–10Ni–3Al–0.8Si alloy during hot compression was about 396.57 kJ/mol.

B. Processing map

Based on the dynamic material modeling,^{15,16} the processing map of hot compressed alloy can be established by calculating the power dissipation efficiency factor and Rheological unstable zone:

$$\eta = \frac{2m}{m+1}, \quad (8)$$

$$\xi(\dot{\epsilon}) = \frac{\partial \ln \left(\frac{m}{m+1} \right)}{\partial \ln \dot{\epsilon}} + m < 0, \quad (9)$$

$$m = \frac{\partial \ln \sigma}{\partial \ln \dot{\epsilon}}, \quad (10)$$

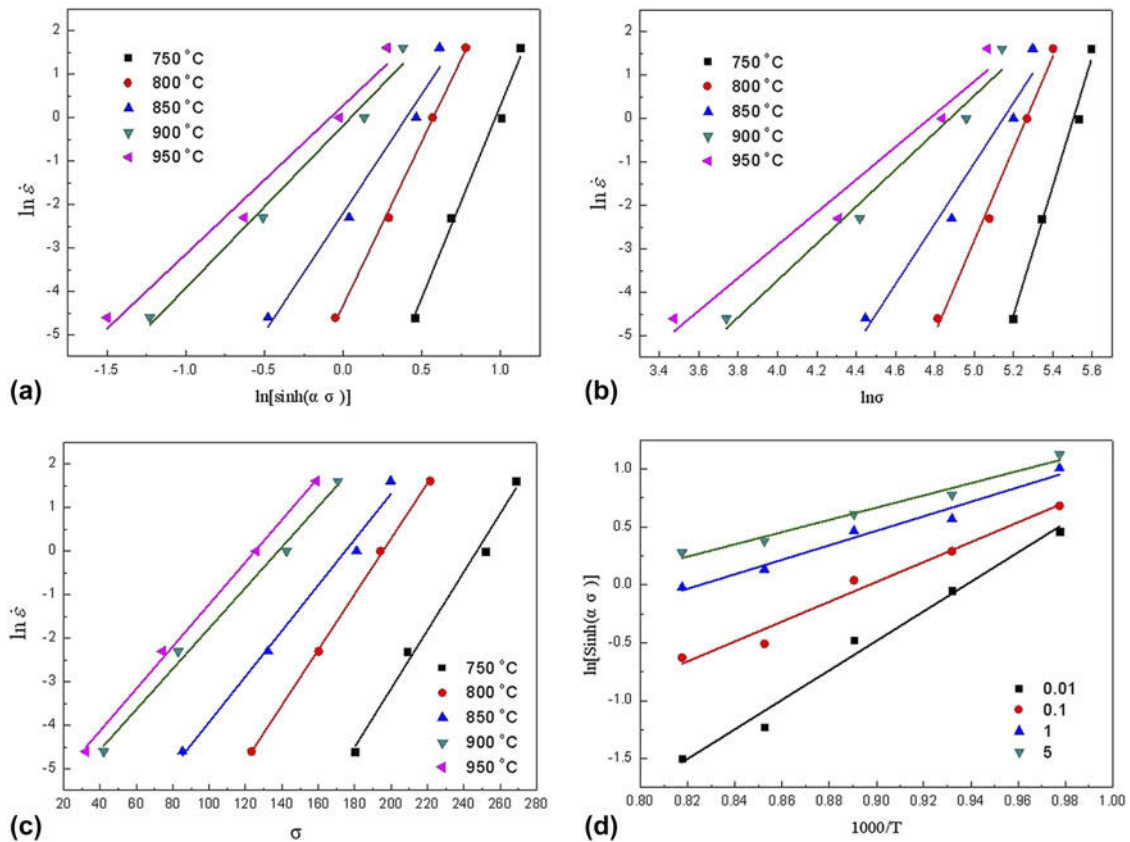


FIG. 2. The (a) $\ln[\sinh(\alpha\sigma)] - \ln \dot{\epsilon}$, (b) $\ln \dot{\epsilon} - \ln \sigma$, (c) $\ln \dot{\epsilon} - \sigma$ and (d) $\ln[\sinh(\alpha\sigma)] - 1000/T$ curves of Cu-10Ni-3Al-0.8Si alloy.

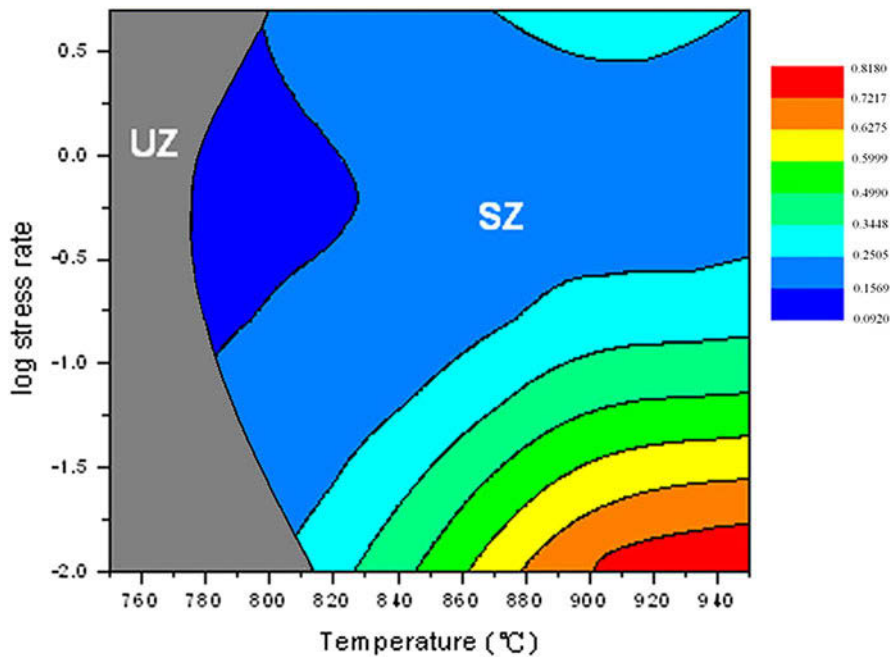


FIG. 3. The processing map of Cu-10Ni-3Al-0.8Si alloy.

where, η is the power dissipation efficiency factor; $\xi(\dot{\epsilon})$ is criterion of Rheological instability; and m is the sensitivity index of strain rate.

Figure 3 shows the processing map with strain rate of 0.6. The hot compression conditions with different power dissipation efficiencies were shown

with different colors. The shaded area presented the Rheological instable zone, indicating that flow stress was unstable when hot compression temperature was below 820 °C. The appropriate compression temperature for Cu–10Ni–3Al–0.8Si alloy was between 900 and 950 °C.

C. Texture evolution

The inverse pole figures of Cu–10Ni–3Al–0.8Si alloy after hot compressed at different temperatures and strain

rates are shown in Fig. 4, and the polar density of each type of texture is shown in Table I. As compressed at 750 °C with low strain rate, the typical texture of hot compressed sample was $\langle 001 \rangle$ and $\langle 011 \rangle$ fiber texture, and the polar density of $\langle 001 \rangle$ and $\langle 011 \rangle$ fiber texture was 3.24 and 3.53, respectively; while, the polar density of $\langle 001 \rangle$ and $\langle 111 \rangle$ fiber texture increased significantly with the increase of temperature, however, that of $\langle 011 \rangle$ and $\langle 112 \rangle$ fiber texture slightly decreased. When the hot compression temperature was fixed, the

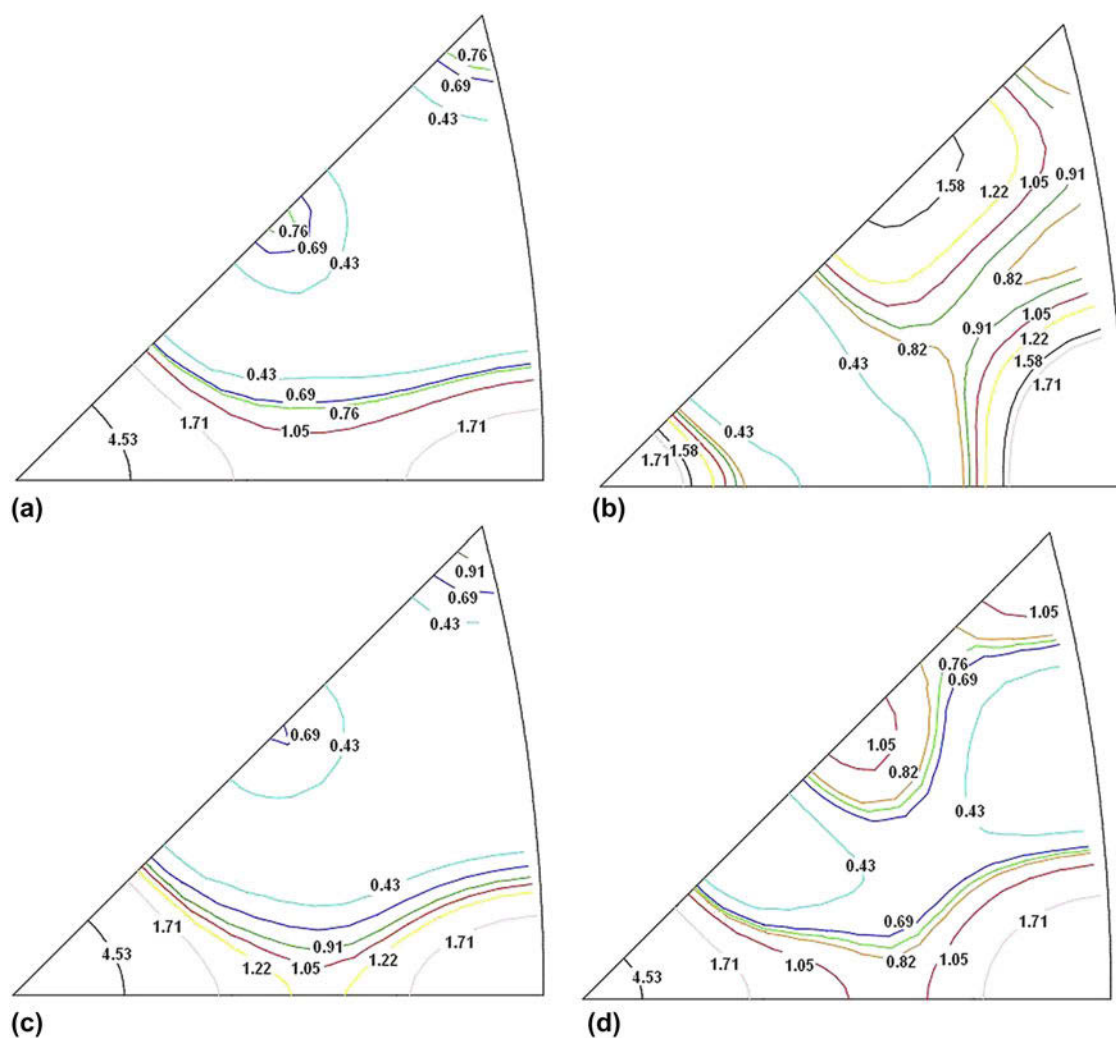


FIG. 4. The inverse pole figures of Cu–10Ni–3Al–0.8Si alloy after hot compressed at different temperatures and strain rates (a) 5 s^{-1} at 750 °C; (b) 0.01 s^{-1} at 750 °C; (c) 5 s^{-1} at 950 °C; (d) 0.01 s^{-1} at 950 °C.

TABLE I. The polar density of texture after hot compressed at different hot compression conditions.

Type of texture	Polar density			
	750 °C 0.01 s^{-1}	750 °C 5 s^{-1}	950 °C 0.01 s^{-1}	950 °C 5 s^{-1}
$\{001\}$	3.24	8.98	6.97	8.96
$\{011\}$	3.53	2.61	3.21	2.72
$\{112\}$	1.70	0.80	1.19	0.71
$\{111\}$	0.58	0.93	1.60	1.01

polar density of $\langle 001 \rangle$ fiber texture decreased and that of $\langle 011 \rangle$ and $\langle 112 \rangle$ fiber texture increased with the decrease of strain rate.

During hot compression, the formation of micro slipping band resulted from the slipping of atomic plans. The accumulation of micro slipping band resulted in the deformation and torsion of the grain. Except for slipping, recrystallization also occurred during hot compression. Both the movement of dislocations and the nucleation of recrystallization are thermal active processes, which increase with the hot compression temperature.¹⁷ When the alloy was hot compressed at 750 °C, the deformation resist force decreased with the decrease of strain rate, then the original grains with $\langle 001 \rangle$ texture rotated easily, resulting in the increase of $\langle 011 \rangle$ texture. As the compression temperature increased to 950 °C, recrystallization was accelerated, as a result, the amount of recrystallization $\langle 001 \rangle$ texture (also the original texture) increased.

D. Microstructure observation

The microstructure of Cu–10Ni–3Al–0.8Si alloy with different hot compression conditions is shown in Fig. 5. DBs formed, while a few recrystallization grains (RGs) were observed in the samples after hot compressed at 750 °C with strain rate of 5 and 0.01 s⁻¹ [Figs. 5(a) and 5(b)]. As the sample hot compressed at 950 °C with strain rate of 5 s⁻¹, RGs nucleated both along the grain boundary and in the grains, while subgrains and DBs were observed in part of the grains [Fig. 5(c)]. When the sample was

compressed at 950 °C with strain rate of 0.01 s⁻¹, RG coarsened rapidly and annealing twins formed, while the amount of subgrains decreased [Fig. 5(d)]. The typical observation OM of the alloy indicated that both recrystallization and recovery were accelerated as the strain rate decreased and temperature increased.

Figure 6 shows the bright field micrographs of the alloy after hot compressed at different temperature with different strain rate. After hot compressed at 750 °C with strain rate of 5 s⁻¹, except for Ni₂Si precipitates, a plenty of dislocations formed in the sample. Those dislocations tangled with each other and interacted with precipitates [Figs. 6(a) and 6(c)], resulting in work hardening and the increase of deformation resisting force. As the amount of dislocations increased to the limits, micro-crack formed, resulting in the crack of the samples. As strain rate decreased to 0.01 s⁻¹, the amount of dislocations decreased, indicating that recovery was accelerated [Fig. 6(b)]. When the sample was hot compressed at 950 °C with strain rate of 5 s⁻¹, only a few Ni₂Si particles precipitated [Figs. 6(d) and 6(f)]. Besides, dynamic discontinuous recrystallization occurred and equiaxed grains with size of about 0.5 μm formed (marked as Grain A); while dislocations remained and subgrain boundaries was observed in part of the grain (marked as Grain B), indicating that continuous recrystallization resulting from recovery occurred [Fig. 6(d)]. Further decreasing strain rate to 0.01 s⁻¹, recrystallization completed [Figs. 6(e) and 5(d)]. Since the amount of precipitates and dislocations decreased while

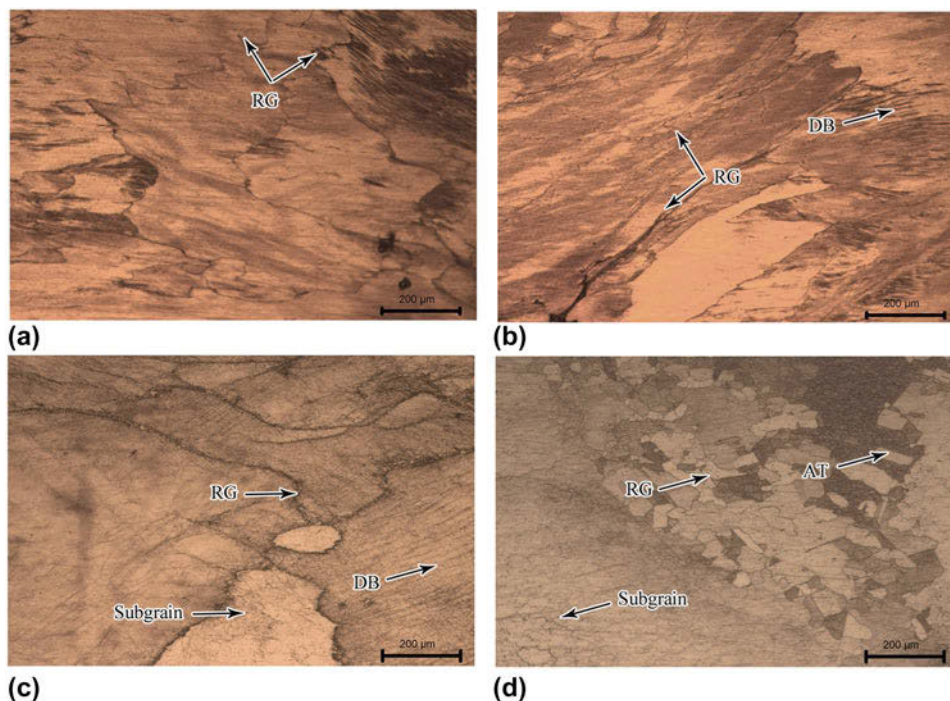


FIG. 5. The microstructure of Cu–10Ni–3Al–0.8Si alloy after hot compressed at different temperatures and strain rates (a) 5 s⁻¹ at 750 °C; (b) 0.01 s⁻¹ at 750 °C; (c) 5 s⁻¹ at 950 °C; (d) 0.01 s⁻¹ at 950 °C.

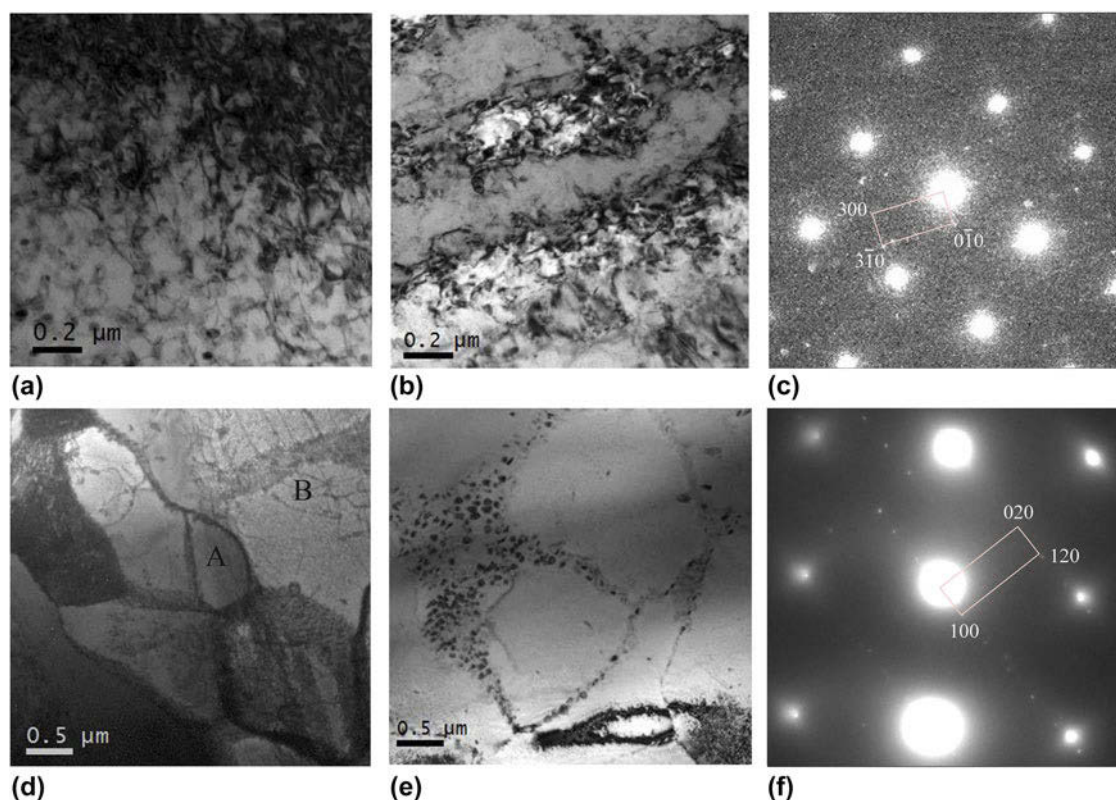


FIG. 6. The TEM micrographs of Cu–10Ni–3Al–0.8Si alloy after hot compressed at different temperatures and strain rates (a) 5 s^{-1} at $750 \text{ }^{\circ}\text{C}$; (b) 0.01 s^{-1} at $750 \text{ }^{\circ}\text{C}$; (c) the SADP of (a); (d) 5 s^{-1} at $950 \text{ }^{\circ}\text{C}$; (e) 0.01 s^{-1} at $950 \text{ }^{\circ}\text{C}$; (f) the SADP of (d).

recrystallization and recovery increased as hot compression temperature increased to $950 \text{ }^{\circ}\text{C}$, the hot deformation resist force decreased.

The EBSD maps of isothermal treated samples after hot compressed at $750 \text{ }^{\circ}\text{C}$ with strain rate of 0.01 and 5 s^{-1} are shown in Fig. 7. Nonuniform deformation occurred in an individual grain and dynamic discontinuous RGs nucleated along the grain boundary in both samples [Figs. 7(a) and 7(c)]. Discontinuous RGs were able to nucleate in the Cu–10Ni–3Al–0.8Si alloy because of its low stacking fault energy.¹⁸ The different parts of the grain rotated and were divided by small-angle boundaries (SAB, rotation angle $<5^{\circ}$) [Figs. 7(b) and 7(d)]. The normal direction of most grains was nearly parallel to $\langle 001 \rangle$ direction. Besides, a plenty of micro-DBs formed in the grains as strain rate increased to 5 s^{-1} [marked with black arrow in Fig. 7(d)], and the average angle between those micro-DBs and compression deformation axis was about 48° . Misorientation was observed across those micro-DBs, as shown in Fig. 7(e). The misorientation accumulated and a continuous rotation exhibited in the grain [Fig. 7(f)], due to the difference of stress in different parts of the grain.

Figures 8(a) and 8(b) present the EBSD observation of isothermal treated alloy after hot compressed at $950 \text{ }^{\circ}\text{C}$ with strain rate of 5 s^{-1} . Compared with the sample hot compressed at $750 \text{ }^{\circ}\text{C}$ with strain rate of 5 s^{-1} , uniform

plastic deformation was observed in the grains after compressed at $950 \text{ }^{\circ}\text{C}$ with the same strain rate. Except for DBs, two types of typical grains were observed, which were marked with grain A and grain B in Fig. 8(a). A plenty of subgrains formed in the grain A with normal direction along $\langle 001 \rangle$; while subgrains with dislocation boundaries formed due to the decrease of deformation resistance and accumulation of a great many of dislocations after hot compressed at evaluated temperature.¹⁹ Besides, small equiaxed grains with large-angle boundary (LAB, rotation angle $>15^{\circ}$) formed in grain B with normal direction along $\langle 111 \rangle$, indicating the nucleation of dynamic discontinuous recrystallization. The average grain size of those discontinuous RGs was about $4 \mu\text{m}$. As strain rate further decreased to 0.01 s^{-1} [Figs. 8(c) and 8(d)], the equiaxed discontinuous RGs without dislocation boundaries grew up to about $20 \mu\text{m}$ (marked with black arrows). Especially, trace of dislocation boundaries was observed in the grain with normal direction along $\langle 001 \rangle$ (marked with grain A'), indicating that the growth of subgrains resulted from the dynamic recovery but out from the nucleus. Such evolution can be referred to dynamic continuous recrystallization.²⁰ The driving force of growth of the subgrains is the decrease of strain-induced energy. The dislocations reacted with each other and encouraged the coalescence of adjacent cells during recovery, leading to increase of the subgrain size and decrease of dislocation boundaries.²¹

To further analyze the influence of hot compression conditions on the evolution of microstructure, the Zener–Hollomon parameter (temperature-corrected

strain rate) Z is applied, which can be expressed in terms of the thermal activation energy, temperature, and strain rate^{22,23}:

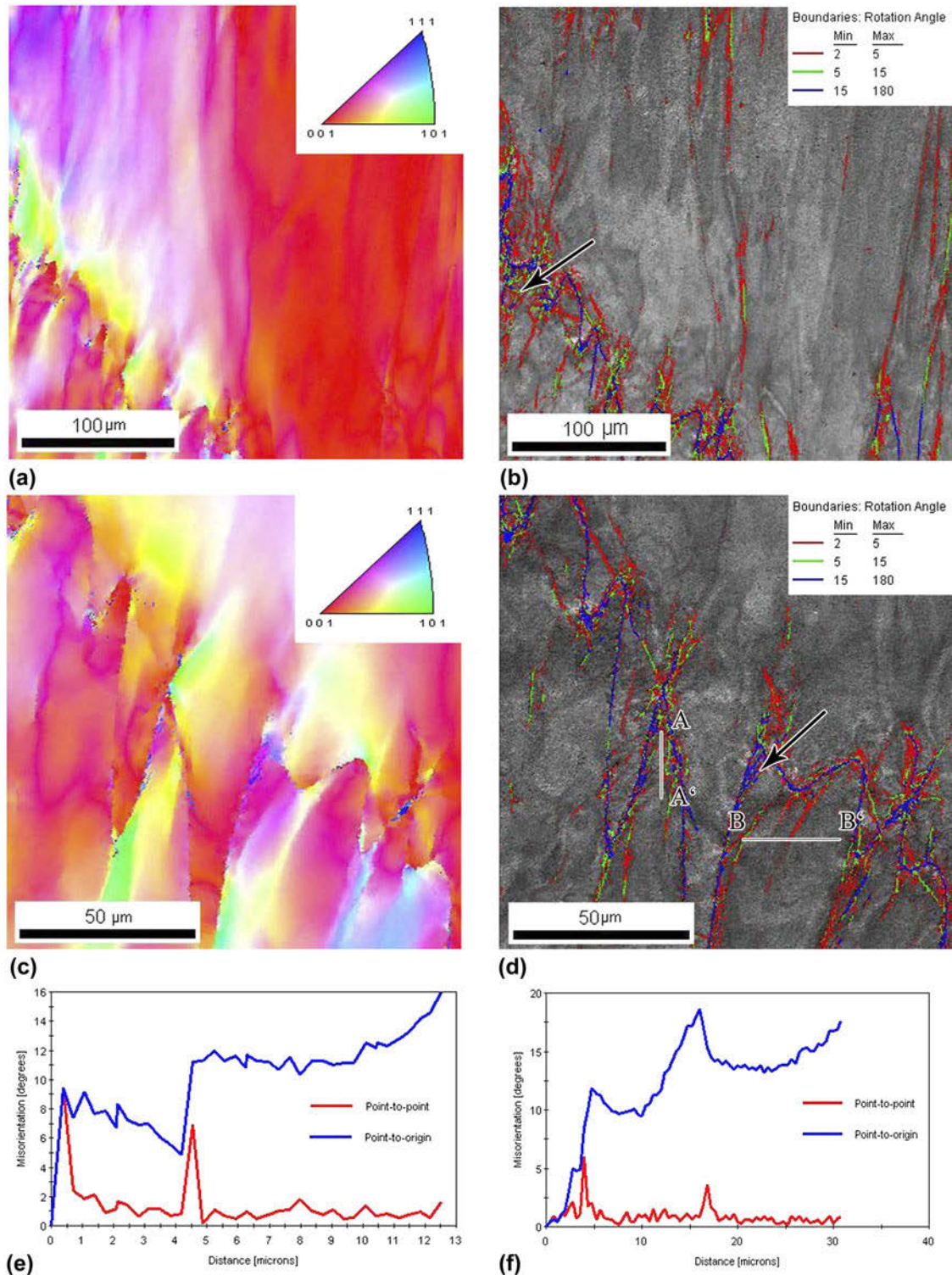


FIG. 7. The EBSD maps of isothermal treated alloy after hot compressed at 750 °C with different strain rate. (a) Orientation map of 0.01 s⁻¹; (b) corresponding Image Quality (IQ) map of 0.01 s⁻¹; (c) orientation map of 5 s⁻¹; (d) corresponding IQ map of 5 s⁻¹; (e) the measured misorientations along A–A’; (f) the measured misorientations along B–B’.

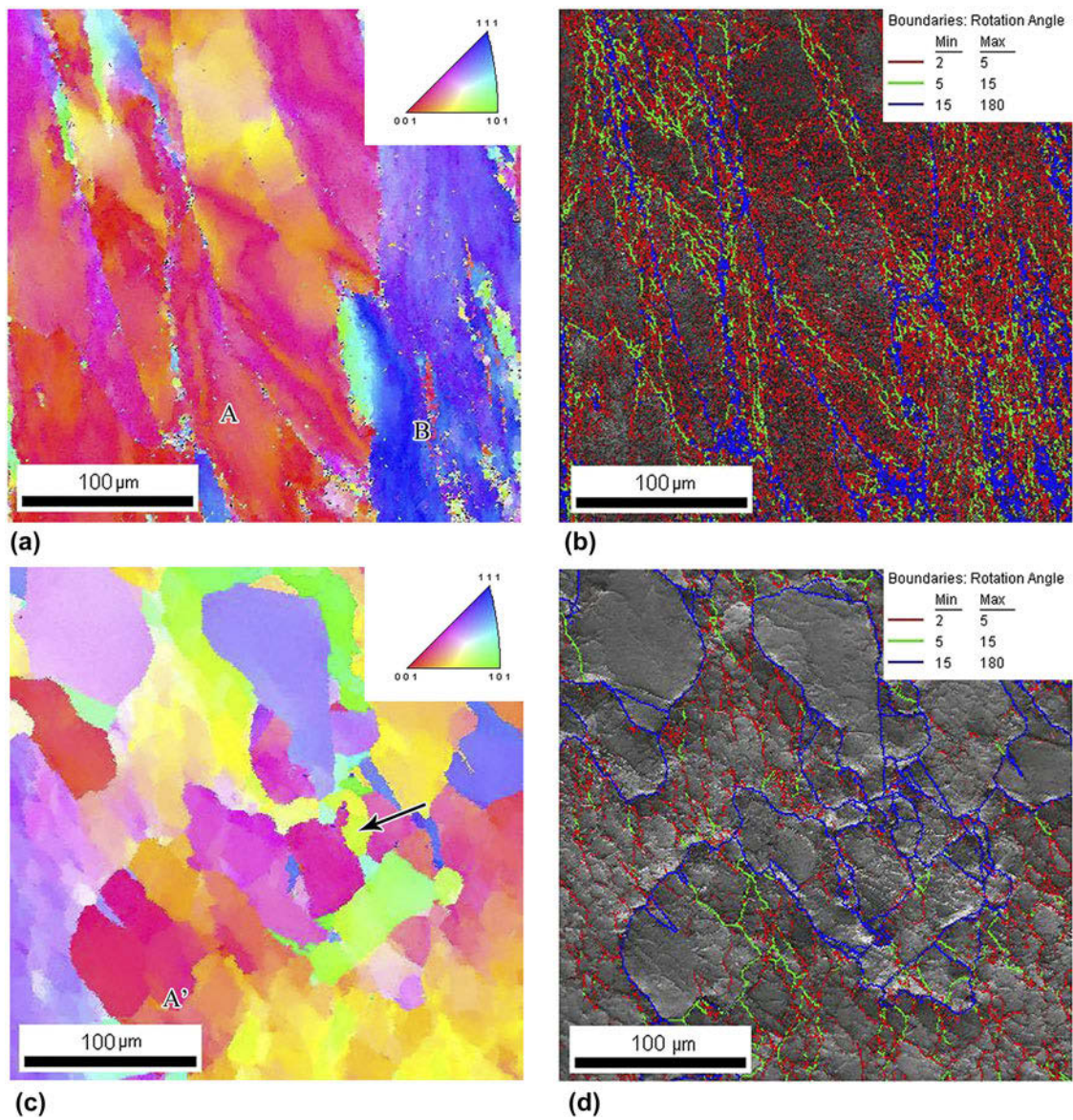


FIG. 8. The EBSD maps of isothermal treated alloy after hot compressed at 950 °C with different strain rates. (a) Orientation map of 5 s⁻¹; (b) corresponding IQ map of 5 s⁻¹; (c) orientation map of 0.01 s⁻¹; (d) corresponding IQ map of 0.01 s⁻¹.

TABLE II. The calculated Zener–Hollomon parameter under different hot compression conditions.

Strain rate (s ⁻¹)	Hot compression temperature (°C)				
	750	800	850	900	950
0.01	1.78 × 10 ¹⁸	2.02 × 10 ¹⁷	2.79 × 10 ¹⁶	4.57 × 10 ¹⁵	8.67 × 10 ¹⁴
0.1	1.78 × 10 ¹⁹	2.02 × 10 ¹⁸	2.79 × 10 ¹⁷	4.57 × 10 ¹⁶	8.67 × 10 ¹⁵
1	1.78 × 10 ²⁰	2.02 × 10 ¹⁹	2.79 × 10 ¹⁸	4.57 × 10 ¹⁷	8.67 × 10 ¹⁶
5	8.88 × 10 ²⁰	1.01 × 10 ²⁰	1.39 × 10 ¹⁹	2.28 × 10 ¹⁸	4.33 × 10 ¹⁷

$$Z = \dot{\epsilon} \exp\left(\frac{Q}{RT}\right) \quad (11)$$

The calculated results of the Zener–Hollomon parameter under different hot compression conditions

are shown in Table II. The Zener–Hollomon parameter of the sample hot compressed at 750 °C with strain rate of 5 s⁻¹ was 8.88 × 10²⁰, while that of the sample compressed at 950 °C with strain rate of 0.01 s⁻¹ decreased to 8.67 × 10¹⁴, indicating that the Zener–Hollomon parameter decreased as

TABLE III. The fraction of boundaries with different misorientation angles under different hot compression conditions.

Hot compression conditions	Z (s ⁻¹)	Fraction of SAB		Fraction of LAB >15°
		2–5°	5–15°	
750 °C 5 s ⁻¹	8.88 × 10 ²⁰	0.626	0.173	0.200
750 °C 0.01 s ⁻¹	1.78 × 10 ¹⁸	0.732	0.151	0.117
950 °C 5 s ⁻¹	4.33 × 10 ¹⁷	0.644	0.167	0.189
950 °C 0.01 s ⁻¹	8.67 × 10 ¹⁴	0.511	0.147	0.342

compression temperature increased or strain rate decreased.

The relationship between the fraction of boundaries with different misorientation angles and Zener–Hollomon parameter is shown in Table III. When the alloy was hot compressed at low temperature, both recovery and discontinuous recrystallization occurred, while the fraction of very small-angle boundary (2–5°) increased as Zener–Hollomon value decreased, indicating that dynamic discontinuous recrystallization was the main softening mechanism of the alloy.²⁴ Further decreasing the Zener–Hollomon value, the fraction of small-angle boundary and dislocation boundaries decreased, while that of large-angle boundary increased and the grain size of subgrains coarsened. The analysis was in accordance with the observation of microstructure [Figs. 5(a), 5(b), 7, and 8]. Continuous recrystallization resulting from dynamic recovery occurred at high temperature.²⁵ Both continuous recrystallization and dynamic discontinuous recrystallization were softening mechanisms of the Cu–10Ni–3Al–0.8Si alloy.

IV. CONCLUSIONS

(1) The true stress increased rapidly at the initial stage of hot compression. After reaching up to the peak values, true stress remained the same or slightly decreased. The peak value of true stress and the Zener–Hollomon parameter decreased with the increase of temperature and decrease of strain rate.

(2) The calculated thermal activation energy of Cu–10Ni–3Al–0.8Si alloy was about 396.57 kJ/mol. The processing map was established and the appropriate compression temperature was between 900 and 950 °C.

(3) The typical texture of hot compressed samples was <001> and <011> fiber texture. Increasing compressing temperature or strain rate, the polar density of <001> fiber texture increased, while that of <011> fiber texture decreased.

(4) Dynamic discontinuous recrystallization nucleated and DBs formed at 750 °C. The formation of continuous recrystallization and equiaxed discontinuous RGs was accelerated with the increase of temperature and the decrease of strain rate.

ACKNOWLEDGMENTS

The work was supported by the Grants from the Project of Innovation-driven Plan in Central South University, the National Natural Science Foundation of China (51271203), the Open-End Fund for the Valuable and Precision Instruments of Central South University (CSUZC201522), the Aid program for Science and Technology Innovative Research Teams in Higher Educational Institutions of Hunan Province, and the State Key Laboratory of Powder Metallurgy of Central South University.

REFERENCES

1. T. Hasegawa, Y. Takagawa, C. Watanabe, and R. Monzen: Deformation of Cu–Be–Co alloys by aging at 593 K. *Mater. Trans.* **52**, 1685 (2011).
2. G-L. Xie, Q-S. Wang, X-J. Mi, B-Q. Xiong, and L-J. Peng: The precipitation behavior and strengthening of a Cu–2.0 wt% Be alloy. *Mater. Sci. Eng., A*, **558**, 326 (2012).
3. Z. Henmi and T. Nagai: Mechanism of precipitation hardening in Cu–Be alloys. *Trans. Jpn. Inst. Met.* **10**, 166 (1969).
4. L-N. Shen, Z. Li, Q-Y. Dong, Z. Xiao, M-Y. Wang, P-H. He, and Q. Lei: Dry wear behavior of ultra-high strength Cu–10Ni–3Al–0.8 Si alloy. *Tribol. Int.* **92**, 544 (2015).
5. L-N. Shen, Z. Li, Q-Y. Dong, Z. Xiao, S. Li, and Q. Lei: Microstructure evolution and quench sensitivity of Cu–10Ni–3Al–0.8Si alloy during isothermal treatment. *J. Mater. Res.* **30**, 736 (2015).
6. S-I. Oh, S-L. Semiatin, and J-J. Jonas: An analysis of the isothermal hot compression test. *Metall. Trans. A* **23**, 963 (1992).
7. R-A. Petkovic, M-J. Luton, and J-J. Jonas: Recovery and recrystallization of polycrystalline copper after hot working. *Acta Metall.* **27**, 1633 (1979).
8. Y. Deng, Z-M. Yin, and J. Huang: Hot deformation behavior and microstructural evolution of homogenized 7050 aluminum alloy during compression at elevated temperature. *Mater. Sci. Eng., A* **528**, 1780 (2011).
9. Q. Lei, Z. Li, J. Wang, S. Li, L. Zhang, and Q-Y. Dong: High-temperature deformation behavior of Cu–6.0Ni–1.0Si–0.5Al–0.15Mg–0.1Cr alloy. *J. Mater. Sci.* **47**, 6034 (2012).
10. D-C. Drucker: Coulomb friction, plasticity, and limit loads, Brown univ. providence ri. div. of applied mathematics, 1953.
11. R. Ebrahimi and A. Najafzadeh: A new method for evaluation of friction in bulk metal forming. *J. Mater. Process. Technol.* **152**, 136 (2004).
12. B. Avitzur: *Metal Forming, Processes and Analysis* (McGraw-Hill, New York, 1968); pp. 102.
13. P. Wanjara, M. Jahazi, H. Monajati, S. Yue, and J-P. Immarigeon: Hot working behavior of near- α alloy IMI834. *Mater. Sci. Eng., A* **396**, 50 (2005).
14. L. Zhang, Z. Li, Q. Lei, W-T. Qiu, and H-T. Luo: Hot deformation behavior of Cu–8.0 Ni–1.8 Si–0.15 Mg alloy. *Mater. Sci. Eng., A* **528**, 1641 (2011).
15. Y. Prasad, H-L. Giegel, S-M. Doraivelu, J-C. Malas, J-T. Morgan, K-A. Lark, and D-R. Barker: Modeling of dynamic material behavior in hot deformation: Forging of Ti-6242. *Metall. Trans. A* **15**, 1883 (1984).
16. S. Anbuselvan and S. Ramanathan: Hot deformation and processing maps of extruded ZE41A magnesium alloy. *Mater. Des.* **31**, 2319 (2010).
17. T. Baudin, A-L. Etter, and R. Penelle: Annealing twin formation and recrystallization study of cold-drawn copper wires from EBSD measurements. *Mater. Charact.* **58**, 947 (2007).

18. Y-H. Zhao, Y-T. Zhu, X-Z. Liao, Z. Horita, and T-G. Langdon: Tailoring stacking fault energy for high ductility and high strength in ultrafine grained Cu and its alloy. *Appl. Phys. Lett.* **89**, 121906 (2006).
19. J-Q. Su, T-W. Nelson, R. Mishra, and M. Mahoney: Microstructural investigation of friction stir welded 7050-T651 aluminium. *Acta Mater.* **51**, 713 (2003).
20. S. Gourdet and F. Montheillet: An experimental study of the recrystallization mechanism during hot deformation of aluminium. *Mater. Sci. Eng., A* **283**, 274 (2000).
21. Q. Lei, Z. Li, J. Wang, J-M. Xie, X. Chen, S. Li, Y. Gao, and L. Li: Hot working behavior of a super high strength Cu–Ni–Si alloy. *Mater. Des.* **51**, 1104 (2013).
22. Y-S. Li, Y. Zhang, N-R. Tao, and K. Lu: Effect of the Zener–Hollomon parameter on the microstructures and mechanical properties of Cu subjected to plastic deformation. *Acta Mater.* **57**, 761 (2003).
23. M. Jafari and A. Najafizadeh: Correlation between Zener–Hollomon parameter and necklace DRX during hot deformation of 316 stainless steel. *Mater. Sci. Eng., A* **501**, 16 (2009).
24. J-C. Tan and M-J. Tan: Dynamic continuous recrystallization characteristics in two stage deformation of Mg–3Al–1Zn alloy sheet. *Mater. Sci. Eng., A* **339**, 124 (2003).
25. S. Gourdet and F. Montheillet: A model of continuous dynamic recrystallization. *Acta Mater.* **51**, 2685 (2003).